# Blind Image Quality Assessment Based on Multi-Channel Features Fusion and Label Transfer

Qingbo Wu, *Member, IEEE,* Hongliang Li, *Senior Member, IEEE,* Fanman Meng, *Member, IEEE,* King N. Ngan, *Fellow, IEEE,* Bing Luo, Chao Huang, and Bing Zeng, *Member, IEEE*

***Abstract*—In this paper, we propose an efficient blind image quality assessment (BIQA) algorithm, which is characterized by a new feature fusion scheme and a *k*-nearest-neighbors (KNN) based quality prediction model. Our goal is to predict the perceptual quality of an image without any prior information of its reference image and distortion type. Since the reference image is unaccessible in many applications, the BIQA is quite desirable under this context. In our method, a new feature fusion scheme is first introduced by combining an image's statistical information from multiple domains (i.e., DCT, wavelet and spatial domains) and multiple color channels (i.e., Y, Cb, Cr). Then, the predicted image quality is generated from a nonparametric model, which is referred to as the label transfer. Based on the assumption that similar images share similar perceptual qualities, we implement the label transfer with an image retrieval procedure, where a query image's KNN are searched for from some annotated images. The weighted average of the KNN labels (e.g., DMOS or MOS) is used as the predicted quality score. The proposed method is straightforward and computationally appealing. Experimental results on three publicly available databases (i.e., LIVE II, TID2008 and CSIQ) show that the proposed method is highly consistent with the human perception and outperforms many representative BIQA metrics.**

***Index Terms*—BIQA, Multi-channel features fusion, Label Transfer.**

## I. Introduction

Digital images are popular in the visual communications, entertainment and social networks. In these fields, an efficient image quality assessment (IQA) algorithm [1], [2] is crucial to evaluate, control and enhance the perceptual image quality. Recently, many objective IQA approaches have been developed. Based on the availability of a reference image, these methods are usually classified into three types: full-reference (FR), reduced-reference (RR) and no-reference/blind (NR). The FR-IQA metrics require full access to the undistorted image and the RR-IQA methods also need partial information from the reference image. By incorporating the spatial domain information, transformation domain information [3], [4] and saliency information [5], [6] into the IQA, many well-established FR [7]–[11] and RR [12], [13] metrics have captured human perception well. However, in many practical applications, the reference image is unavailable (e.g., image restoration, etc.), which limits the application fields of the FR and RR IQA algorithms. In contrast, the NR/Blind-IQA method does not need the information of the reference image, which is appealing and quite challenging.

Most existing BIQA approaches are composed of two modules: 1) Quality-aware feature extraction. This module generates an efficient image representation to capture the perceptual quality variation caused by the distortion. As discussed in [2], [14]–[17], many BIQA methods focus on describing an image based on its natural scene statistics (NSS) from the single color channel (i.e., the grayscale map). These NSS are extracted from different domains, e.g., the BLINDS-II [15] focuses on the DCT domain, the DIIVINE [16] works on the wavelet domain and the NIQE [17] is executed on the spatial domain. 2) Prediction model learning. This module is mainly used to map the image features to the subjective quality scores. In many BIQA algorithms [15], [16], [18]–[20], the learning-based regression models are widely used, such as the support vector regression (SVR) [21] and the general regression neural network (GRNN) [22], etc.

Although the aforementioned methods have achieved promising results, many important characteristics of the visual perception are still underutilized. 1) In the feature extraction module, many existing methods extract the single-domain features, which are not sufficient to simulate the complex visual perception mechanism. The multi-domain information in both the spatial and spatial-frequency domains is necessary to precisely represent an image in the visual cortex [23], [24]. Moreover, the multi-channel color information is rarely discussed for the BIQA task. As discussed in [25], we know that the trichromacy is an important underlying property of the human vision system. 2) In the quality prediction module, there are also two common issues. Firstly, the learning-based methods are dataset dependent. When the training samples are changed, the model parameters need to be retrained. Secondly,



Manuscript received March 17, 2014. This work was supported in part by the National Basic Research Program of China (973 Program 2015CB351804), National Natural Science Foundation of China (No. 61271289), The Ph.D. Programs Foundation of Ministry of Education of China (No. 20110185110002) and by The Program for Young Scholars Scientific and Technological Innovative Research Team of Sichuan Province, China (No. 2014TD0006).

Q. Wu, H. Li, F. Meng, B. Luo and C. Huang are with School of Electronic Engineering, University of Electronic Science and Technology of China, Chengdu 611731, China (e-mail: wqb.uestc@gmail.com; hlli@uestc.edu.cn; fmmeng@uestc.edu.cn; Mathild1987@163.com; huangchao_uestc@aliyun.com).

K. N. Ngan is with Department of Electronic Engineering, The Chinese University of Hong Kong, ShaTin, Hong Kong, and School of Electronic Engineering, University of Electronic Science and Technology of China, Chengdu 611731, China (e-mail: knngan@ee.cuhk.edu.hk).

B. Zeng is with School of Electronic Engineering, University of Electronic Science and Technology of China, Chengdu, China, and Department of Electronic and Computer Engineering, The Hong Kong University of Science and Technology, Kowloon, Hong Kong (e-mail:eezeng@uestc.edu.cn).

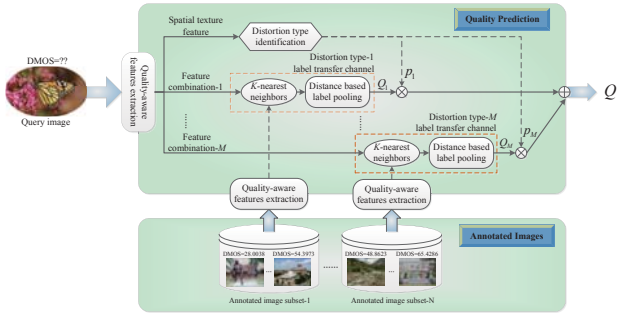


Fig. 1. The framework of our proposed TCLT method.

these regression models (e.g., SVR and GRNN) usually work like the black box mapping, which can't provide an intuitive visual perception interpretation for the BIQA.

To address the problems mentioned above, we propose a novel BIQA algorithm which is extended from our previous work [26]. Particularly, we introduce the multi-domain/channel information to capture the hierarchical and trichromatic properties which are lost in the single-domain/channel features. Meanwhile, a label transfer method is proposed to intuitively simulate the visual memory retrieval process in the BIQA. In comparison with [26], the visual perception properties behind each proposed feature are further explored here. More extensive experiments and application instance are added to evaluate the proposed method. Meanwhile, the computational complexity of our method is investigated as well.

In view of the superiority of capturing different NSS characteristics under each distortion type, we follow the two-step scheme in [16], [19] and implement the BIQA with the distortion type classification and label transfer (TCLT). Inspired by the human perception properties, many new elements are introduced into the proposed method, i.e.,

1) Multiple-domain features are introduced to simulate the hierarchical structure of the visual cortex perception [27], [28], which combine the DCT, wavelet and spatial domains information to compensate the visual information lost in the single domain.
2) In view of the trichromatic property of the human color vision [25], a multi-channel fusion scheme is developed by combining the NSS information from all of the YCbCr color channels.
3) In [17], Mittal *et al.* proposed a novel "completely blind" metric which estimates a query image's quality by measuring its difference with the pristine images in terms of the multivariate Gaussian (MVG) model-based NSS feature. Inspired by this work, we develop a label transfer method to transfer the DMOS labels from some annotated samples to the query image. Based on the assumption that the images with similar quality-aware features share similar perceptual qualities, we utilize the feature distance to search for query image's KNN and compute specific weights for each query image. Then, the weighted average of the KNN's DMOS labels is used as the predicted perceptual quality.

The framework of our proposed method is shown in Fig. 1. Firstly, a SVM classifier is used to identify the query image's probabilities of belonging to each distortion type, which are denoted by $p_1$ to $p_M$. Secondly, the distortion-specific label transfer is implemented in each annotated image subset, whose samples share the same distortion type. The predicted qualities in each label transfer channel are denoted by $Q_1$ to $Q_M$. Finally, the weighted average of $Q_1$ to $Q_M$ is used as our perceptual quality score $Q$. Extensive experiments on the LIVE II [29], TID2008 [30] and CSIQ [31] databases show that the proposed method is remarkably consistent with the human perception and outperforms many state-of-the-art BIQA metrics.

The remainder of this paper is organized as follows. Section II describes the proposed multi-channel fusion features. Section III presents the label transfer-based quality prediction model. Experimental results are shown in section IV. Then, an image auto-denoising application is discussed in section V. Finally, the conclusion is drawn in section VI.

## II. Multi-channel Fusion Features

Our crucial idea is to match perceptually similar images. Thanks to the developments of neural science and visual cognition theories, many neurophysiological evidences have been found to reveal the visual perception process.

It is verified that the visual perception system is highly hierarchical, i.e., the local low-level image features are extracted in the neurons of the early visual area and the more complex features will be produced in the higher visual areas. Here, we investigate the properties of areas V1 and V2, which are highly correlated with the visual description in the primate neocortex [27], [28]. Then, the multi-channel fusion features in multiple domains are introduced to simulate this perception structure.

### A. Quality-aware Features for Visual Area V1

As described in [27], [28], V1 is the first visual perception cortical area, which is sensitive to simple local features, e.g., edges, bars, spatial frequency, etc. Correspondingly, the DCT is a practical tool to represent the local patch with its responses to some orthogonal basis functions, which capture different spatial frequency and local structures [32], [33].

It is noted that human perception presents different sensitivities for different spatial frequencies [27], [33]. Thus, we focus on investigating the NSS of the normalized frequency band coefficient $c_i$ in each band. Let $f_i(x,y)$ denote an element in the $x$th row, $y$th column of the DCT coefficient matrix and its frequency band is $i$. Then, we can get

$$c_i = \sqrt{\frac{1}{N_i}\sum_{x,y\in U_i} f_i^2(x,y)} \qquad (1)$$
$$U_i = \{x,y | x+y=i, 0\le x<W, 0\le y<W\}$$

where $N_i$ is the number of DCT coefficients in the $i$th frequency band, $W$ is the size of the coefficient matrix. An instance of the frequency bands locations for a $4\times 4$ block is illustrated in Fig. 2, where the coefficients in the same frequency band are labeled with the same intensity and texture.

Here, we try to develop quality-aware indexes from the DCT domain. Similar works can be found in [14], [15]. The

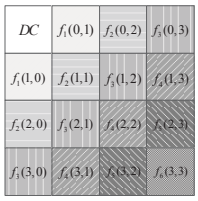


Fig. 2. The frequency bands in the 4×4 DCT domain.

TABLE I
COMPARISON BETWEEN THE PROPOSED DCT FEATURES AND THE OTHER METHODS

| | Full-band | Band-wise | Multi-channel |
|---|---|---|---|
| [14] | Mean value, Kurtosis | Renyi-Entropy | × |
| [15] | GGD shape parameter, Variance/Mean | Energy Difference, Multi-orientation Variance/Mean | × |
| Proposed | Skewness | Shannon-Entropy, Difference Shannon-Entropy | ✓ |

BLINDS [14] describes the local contrast, zero coefficient peakness and the directional information loss in the DCT domain. The BLINDS-II [15] extracts the DCT coefficients' shape parameter, the frequency variation and the relative distribution between the higher and the lower bands.

Since the human vision tends to represent the image with minimal redundancy [34], we explore the quality-aware DCT features from the coding related cues, which is different from previous works. As discussed in [35], the NSS mainly concentrates on the intrablock and interblock correlations in the DCT domain. Here, we develop three DCT domain indices to capture these correlation properties. The detailed comparison between the proposed DCT features and [14], [15] is shown in Table I, where the full-band denotes the statistics on all DCT coefficients and the band-wise denotes the statistics in each frequency band. In the full-band, we only use the skewness to describe the intrablock correlation and [14], [15] introduce more information, such as, mean, variance, kurtosis and GGD shape parameter. In the band-wise, we compute two kinds of Shannon entropies on the normalized frequency band coefficients, which doesn't consider the correlation in different orientations like [15]. In addition, as shown in Table I, only our DCT features introduce the multi-channel color information, which is not considered for both [14] and [15].

*1) The Intrablock DCT Feature:* In the DCT domain, a well-known feature for the natural image is its energy decay property as the frequency increases in the intrablock [35]. When the annoying distortion is present, the decay rate of the frequency band coefficients' distribution will change accordingly. Here, the distribution of the intrablock skewness [36] is computed to measure this statistical variation.

Let $\mathcal{C}^j$ denote the frequency band coefficient set in the $j$th block, where $\mathcal{C}^j = \{c_1^j, \cdots, c_{N_c}^j\}$ and $N_c$ is the number of the frequency bands in a block. In our experiment, the DCT is implemented on each non-overlapped $8 \times 8$ block, which makes $N_c$ up to 14. Then, the $j$th block's skewness $s^j$ is

$$s^j = \frac{E(\mathcal{C}^j - \mu(\mathcal{C}^j))^3}{\sigma^3(\mathcal{C}^j)} \tag{2}$$

where $\mu(\cdot)$ is the mean value operator, $\sigma(\cdot)$ is the standard deviation operator and $E(\cdot)$ is the expectation operator.

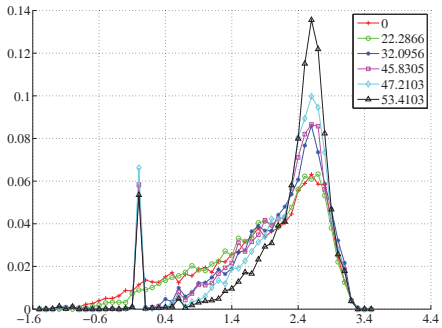


Fig. 3. The distributions of the intrablock skewness for the images with different DMOS. The x-axis indicates the available skewness values, and the y-axis indicates the distribution probability of each skewness value. Legend: the DMOS value of each image.

To obtain the global descriptor, we compute the intrablock skewness distribution across all blocks. Let $\mathcal{S}$ denote the intrablock skewness set, where $\mathcal{S} = \{s^1, \cdots, s^{N_b}\}$ and $N_b$ is the blocks' number. Then, its margin distribution $P(\mathcal{S})$ is

$$P(\mathcal{S}) = norm(hist(\mathcal{S})) \tag{3}$$

where $hist(\cdot)$ is the histogram operator and $norm(\cdot)$ represents the $l1$-normalization, i.e., $norm(x) = x/\|x\|_1$. Here, the dimension of $P(\mathcal{S})$ is set to 51 based on our experimental study, which could achieve good quality prediction accuracy.

To illustrate the distortion impact for the intrablock skewness, an instance is shown in Fig. 3, where the curves with different colors denote the $P(\mathcal{S})$ extracted from the luma components of the image *monarch* and its five JP2K versions. A higher skewness indicates a more intensive mass distribution on the left of the mean value, which is induced by a faster decay rate. It is clear that the perceptual quality degradation could be efficiently captured by $\mathcal{P}(\mathcal{S})$, where different image qualities correspond to different distributions. For the severely distorted images labeled by larger DMOS, their $\mathcal{P}(\mathcal{S})$ would be more focused on higher values. For the slightly distorted images with smaller DMOS, their $\mathcal{P}(\mathcal{S})$ are more smooth and spread on many low value bins. Since the JP2K introduces the high frequency loss, it accelerates the energy decay for the intrablock DCT coefficients. We can measure two images' perceptual similarity by computing their $P(\mathcal{S})$ feature distance, where the more similar images have a smaller distance.

*2) The Interblock DCT Feature:* It is verified that human vision tends to present natural scenes with minimal redundancy [34], [37]. The image distortions often modify the amount of image information by smoothing local structure or adding random noise. To measure this variation, two entropy-based indices are introduced here.

Firstly, let $\mathcal{C}_i$ denote the coefficient set of the $i$th frequency band across all blocks, where $\mathcal{C}_i = \{c_i^1, \cdots, c_i^{N_b}\}$. Then, the $i$th band's shannon entropy [38] $e_i$ is defined as

$$e_i = E[-\log_2(P(\mathcal{C}_i))] \tag{4}$$

where $P(\mathcal{C}_i) = norm(hist(\mathcal{C}_i))$. In our experiment, we quantize the $\mathcal{C}_i$ into 500 bins in computing its histogram.

The global frequency band entropy feature is represented as

$$E = [e_1, e_2, \cdots, e_{N_c}] \tag{5}$$

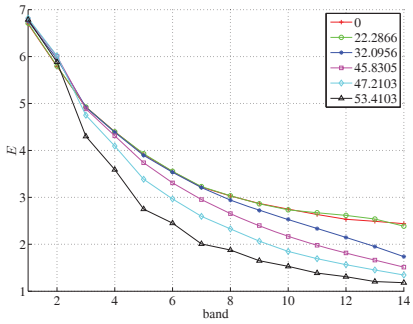


Fig. 4. The distribution of the DCT entropy feature versus the frequency band. The x-axis indicates the frequency band in the DCT domain, and the y-axis indicates the corresponding frequency band entropy. Legend: the DMOS value of each image.

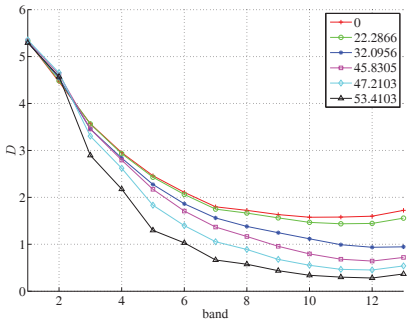


Fig. 5. The distribution of the DCT inter-band difference entropy feature versus the frequency band. The x-axis indicates the frequency band in the DCT domain, and the y-axis indicates the corresponding inter-band difference entropy. Legend: the DMOS value of each image.

An instance of the distortion impact for $E$ is illustrated in Fig. 4, where different curves correspond to the $E$ extracted from the luma components of the image *monarch* and its five JP2K versions. Similar to the intrablock energy compaction property [39], we can find an entropy decay trend as the DCT frequency band increases in the interblock statistics. This is because the natural images have higher responses to the low-frequency DCT basis functions. When the local image structures vary from one block to another one, the low-frequency coefficients exhibit larger dynamic range and decentralized distribution. In contrast, the high-frequency coefficients are usually very small and gather around zero. When the JP2K compression is introduced, there are more high-frequency coefficients quantized to zero, which further accelerates the entropy decay as shown in Fig. 4.

Secondly, to pop out the distortion effect under diverse image contents [40], we further compute the entropy for the difference $g_i$ of the neighboring frequency bands' coefficients

$$g_i = c_i - c_{i+1} \tag{6}$$

Let $\mathcal{G}_i$ denote the difference set between the $i$th and $(i+1)$th frequency bands' coefficients across all blocks, where $\mathcal{G}_i = \{g_i^1, \cdots, g_i^{N_b}\}$. The entropy of $\mathcal{G}_i$ can be represented as

$$d_i = E[-\log_2(P(\mathcal{G}_i))] \tag{7}$$

where $P(\mathcal{G}_i) = norm(hist(\mathcal{G}_i))$. Similar to (4), the histogram bins of $hist(\mathcal{G}_i)$ are also set to 500.

By combining the inter-band difference entropy of all frequency bands, we can obtain the second interblock feature

$$D = [d_1, d_2, \cdots, d_{N_c-1}] \tag{8}$$

In Fig. 5, we show an instance to illustrate the distortion impact on feature $D$, where different curves denote the $D$ extracted from the luma components of the image *monarch* and its five JP2K versions. It can be seen that all curves associated with different DMOS show different distributions. Meanwhile, a larger DMOS shows a greater difference with respect to the undistorted image. Similar to $E$, the feature $D$ also presents the energy decay trend as the frequency increases, which is caused by the nonlinear amplitude decay of the spatial frequency responses for the natural images [37]. Since the low-frequency bands have faster decay rate, the dynamic range of their difference is larger relative to the high-frequency bands. When the JP2K compression is applied, the small coefficients in the high-frequency bands are more easily eliminated, which enlarges the difference between the high-frequency and low-frequency bands and increases the decay rate.

### B. Quality-aware Features for Visual Area V2

As discussed in [41], the visual area V2 contains two features. One focuses on capturing the localized, oriented and bandpass information like area V1. The other one represents more complex position and scale invariance and is sensitive to the shape and texture information [42]. To describe these properties, we develop two statistical indices in the wavelet domain and spatial domain, respectively.

*1) Multiscale and multidirection information in the wavelet domain:* Due to the inherent multiscale and multidirection properties, the wavelet transform is widely used to simulate the visual cortex property [16]. The wavelet decomposition is usually implemented in a multiscale steerable pyramid structure along the horizontal, vertical and diagonal directions, which are denoted by HL, LH and HH respectively. Here, the wavelet decomposition scale is set to 4 based on our experimental study, which could achieve good quality prediction accuracy.

In the wavelet domain, there are two important statistical properties for natural images, i.e., exponential decay and self-similarity across all scales [43], [44]. When distortion is introduced, the deviation will arise in these statistics. Here, we develop two statistical indices to describe these properties.

Firstly, we employ the entropy of each subband to quantitatively measure the exponential decay property. Here, we decompose each channel of a color image into $L$ scales with the wavelet transform. Let $\hat{e}_{k,l}$ denote the entropy of a subband in the $k$th direction and the $l$th scale, where $1 \leq l \leq L$ and $k = \{1, 2, 3\}$ correspond to the HL, LH and HH directions, respectively. Then, the definition of $\hat{e}_{k,l}$ can be given by

$$\hat{e}_{k,l} = E[-\log_2(P(\mathcal{X}_{k,l}))] \tag{9}$$

where $\mathcal{X}_{k,l}$ denotes the wavelet coefficient set in the $k$th direction and $l$th scale, $P(\mathcal{X}_{k,l}) = norm(hist(\mathcal{X}_{k,l}))$. The bin number of $hist(\mathcal{X}_{k,l})$ is set to 800 based on our experimental study, which could achieve good quality prediction accuracy.

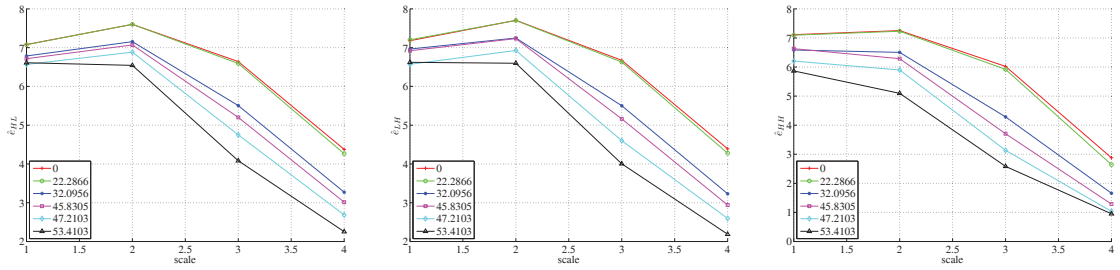


(a) HL (b) LH (c) HH

Fig. 6. Distributions of wavelet entropy under different subbands. The x-axis indicates the scale in each subband and the y-axis indicates the entropy of the wavelet coefficients. Legend: the DMOS of each image.

To capture the exponential decay properties under different directions, we collect three directional subband entropies, i.e.,

$$\begin{aligned}\hat{e}_{HL} &= [\hat{e}_{1,1}, \hat{e}_{1,2}, \cdots, \hat{e}_{1,L}] \\ \hat{e}_{LH} &= [\hat{e}_{2,1}, \hat{e}_{2,2}, \cdots, \hat{e}_{2,L}] \\ \hat{e}_{HH} &= [\hat{e}_{3,1}, \hat{e}_{3,2}, \cdots, \hat{e}_{3,L}]\end{aligned} \tag{10}$$

where $\hat{E} = [\hat{e}_{HL}, \hat{e}_{LH}, \hat{e}_{HH}]$ is defined as the overall wavelet entropy feature and its dimension is $3 \times L$.

Fig. 6 shows the instances of the distortion impact on $\hat{e}_{HL}, \hat{e}_{LH}$ and $\hat{e}_{HH}$, where different curves correspond to the wavelet entropy features extracted from the luma components of the image *monarch* and its five JP2K versions. It is clear that the curves associated with different perceptual qualities separate from each other. The curves associated with larger DMOS are farther from the undistorted image's curve. In all three directions, the subband entropies present a regular decay trend from the coarse scale to the finer one. When the JP2K compression is present, the low-value coefficients on the finer scales are more easily quantized to zero, which causes a higher entropy decay rate as shown in Fig. 6.

Secondly, the self-similarity property indicates that the wavelet coefficients are strongly correlated across all scales, which is usually referred to as "inter-subband correlation" [45]. In [16], the authors try to measure this property with the structural similarities among different wavelet subbands, where the spatial information is considered in locating the comparison windows. In this work, we only consider the difference of the frequency distribution across the neighboring scales and the Kullback-Leibler divergence (KLD) [38] is employed to measure it. Let $\hat{d}_{k,l}$ denote the neighboring subbands' KLD between the $l$th and the $(l+1)$th scale along the $k$th direction. Then, its definition can be given by

$$\hat{d}_{k,l} = E_{P(\mathcal{X}_{k,l+1})}\Big[\log_2\big(\frac{P(\mathcal{X}_{k,l+1})}{P(\mathcal{X}_{k,l})}\big)\Big] \tag{11}$$

where a larger $\hat{d}_{k,l}$ indicates weaker similarity between two neighboring subbands.

Similar to our entropy features, the KLD features are also computed in three individual directions, i.e.,

$$\begin{aligned}\hat{d}_{HL} &= [\hat{d}_{1,1}, \hat{d}_{1,2}, \cdots, \hat{d}_{1,L-1}] \\ \hat{d}_{LH} &= [\hat{d}_{2,1}, \hat{d}_{2,2}, \cdots, \hat{d}_{2,L-1}] \\ \hat{d}_{HH} &= [\hat{d}_{3,1}, \hat{d}_{3,2}, \cdots, \hat{d}_{3,L-1}]\end{aligned} \tag{12}$$

where $\hat{D} = [\hat{d}_{HL}, \hat{d}_{LH}, \hat{d}_{HH}]$ is defined as the overall wavelet inter-subband KLD feature and its dimension is $3 \times (L-1)$.

The instances of the distortion impact on $\hat{d}_{HL}, \hat{d}_{LH}$, and $\hat{d}_{HH}$ are shown in Fig. 7, where different curves denote the inter-subband KLD features extracted from the luma components of the image *monarch* and its five JP2K versions. In all directions, the curves associated with different DMOS present different distributions. The seriously distorted image show higher inter-subband KLD than the clear image in the mid-scale. However, an opposite case arises in the fine-scale. It is noted that the mid-scale $\hat{d}_{k,l}$ measures the inter-subband correlation between the coarse-scale and the fine-scale. Since the magnitudes of the coarse-scale coefficients are higher than the one in the fine-scale, the information loss caused by JP2K is imbalanced in the two scales, which increases the inter-subband difference. In contrast, the fine-scale $\hat{d}_{k,l}$ corresponds to two subbands in the finer scales. The JP2K tends to suppress the low value coefficients, which makes the coefficient distributions of these two scales more consistent.

*2) Texture information in the spatial domain:* As discussed in [46], [47], most cells in area V2 possess the cue-invariant responses for the texture. To capture this property, we use the local binary pattern (LBP) [48] descriptor, which has gray-scale and rotation invariance. As discussed in [48], we know that LBP can obtain good texture classification performance with 16 neighbors in the radius of 2. A larger neighbor and the radius may slightly increase its classification accuracy. However, the feature dimension would become higher, which increases the complexity in computing the feature distance. Thus, we set the radius to 2 and use 16 neighbors in computing the LBP$^{ri}$ feature, whose dimension is 4116.

### C. Multi-channel Fusion for Trichromatic Property

We introduce the multi-channel fusion features based on two factors. Firstly, the human vision has an inherent trichromatic property [25]. Secondly, some image distortions may present different degradation degrees in each color channel. For example, the JPEG and JP2K use different quantization and entropy coding settings for the luma and chroma channels.

Here, we use the YCbCr color space for its superiority in matching the human perception and the low complexity in color space transformation [49]. Since the Cb and Cr components present strong correlation [50], the same features are extracted from them. The multi-channel fusion features can be obtained by combining the NSS from all color channels.

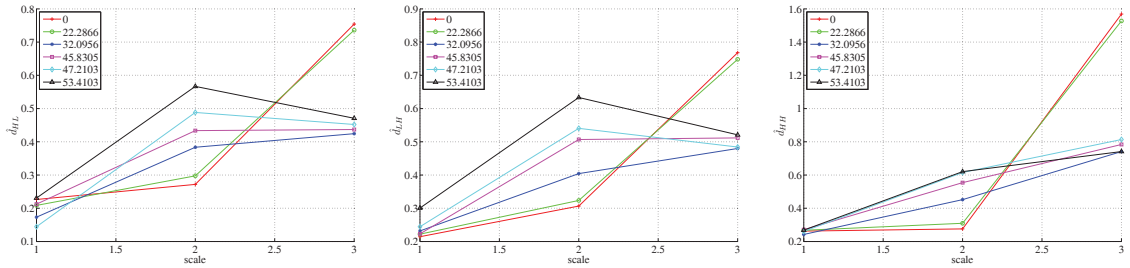


(a) HL (b) LH (c) HH

Fig. 7. Distributions of wavelet KLD under different subbands. The x-axis indicates the scale in each subband and the y-axis indicates the KLD of two neighboring wavelet subbands. Legend: the DMOS value of each image.

Here, the DCT domain multi-channel fusion features are

$$\begin{aligned}\mathcal{P} &= [P^Y(\mathcal{S}), P^{Cb}(\mathcal{S}), P^{Cr}(\mathcal{S})] \\ \mathcal{E} &= [E^Y, E^{Cb}, E^{Cr}] \\ \mathcal{D} &= [D^Y, D^{Cb}, D^{Cr}]\end{aligned} \tag{13}$$

where the dimensions of $\mathcal{P}$, $\mathcal{E}$ and $\mathcal{D}$ increase to $3\times51$, $3\times14$ and $3\times13$, respectively.

The wavelet domain multi-channel features are

$$\begin{aligned}\hat{\mathcal{E}} &= [\hat{E}^Y, \hat{E}^{Cb}, \hat{E}^{Cr}] \\ \hat{\mathcal{D}} &= [\hat{D}^Y, \hat{D}^{Cb}, \hat{D}^{Cr}]\end{aligned} \tag{14}$$

where the dimensions of $\hat{\mathcal{E}}$ and $\hat{\mathcal{D}}$ increase to $3\times3\times4$ and $3\times3\times3$, respectively.

In the spatial domain, we capture the texture variation caused by the distortion. However, most regions in the chroma components are smooth. Since the LBP loses the magnitude of the local contrast, many small noise in the chroma components will reduce its discriminative power. Accordingly, we only extract the LBP feature in the luma component.

### D. The Validity Analysis

Here, we further give a quantitative analysis to verify the validity of our proposed features, i.e., whether the close samples in our proposed feature space share the similar subjective qualities. We implement a simple nearest neighbor quality prediction on the LIVE II database, where one of 29 reference images and its distorted versions are used as the testing set. The rest of the images are used as the training set.

In the testing stage, we estimate the query image subjective quality with the DMOS of an annotated image, whose feature has the minimum chi-square distance with respect to it. For each proposed feature, we repeat the random non-overlapped train-test trials 100 times. Finally, the median SROCC between the predicted qualities and their ground-truth DMOS across the 100 trials are reported in Table II, where each row corresponds to the performance of one proposed feature.

It can be seen that our proposed features work well in measuring the images' perceptual similarity. Based on a simple nearest neighbor estimation, we can efficiently predict the test images' quality ranks, where all features' median SROCC are larger than 0.8 across different distortion types. To verify the validity of our composite features, we investigate the performances of the feature combinations based on the greedy search [51], where the composite features' number $N_f$ can range from 1 to 6. When $N_f$ is larger than one, we use the product of multiple feature distances to measure perceptual similarity. Here, the investigation result is shown in Fig. 8. It can be seen that the median SROCC steadily increases as we add the number of the composite features. That is, our composite features could measure the perceptual similarity more accurately. In addition, since there is no content overlap between the training set and testing set, we can safely conclude that the proposed features could accurately measure the perceptual similarity across different image contents.

TABLE II
THE MEDIAN SROCC ACROSS 100 TRAIN-TEST TRIALS BASED ON THE NEAREST NEIGHBOR QUALITY ESTIMATION.

| | JP2K | JPEG | WN | Blur | FF | All |
|---|---|---|---|---|---|---|
| $\mathcal{P}$ | 0.9000 | 0.9429 | 0.9000 | 0.9747 | 0.8944 | 0.8742 |
| $\mathcal{E}$ | 0.8857 | 0.9276 | 1.000 | 0.9000 | 0.8000 | 0.8538 |
| $\mathcal{D}$ | 0.8117 | 0.9009 | 1.000 | 0.9000 | 0.8000 | 0.8431 |
| $\hat{\mathcal{E}}$ | 0.9258 | 0.8944 | 1.000 | 1.000 | 0.8944 | 0.8868 |
| $\hat{\mathcal{D}}$ | 0.8986 | 0.8286 | 0.9747 | 0.9747 | 0.8721 | 0.8673 |
| LBP | 0.8857 | 0.9276 | 1.000 | 0.9747 | 0.8944 | 0.8670 |

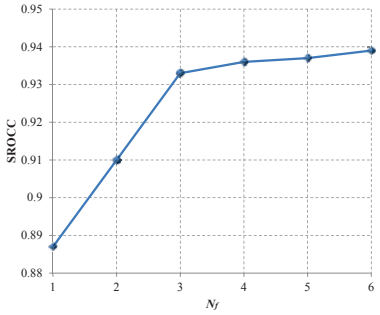


Fig. 8. The plot of the median SROCC vs. the number of proposed features.

## III. Prediction Model based on Label Transfer

As discussed in [52], [53], the visual memory and perception are highly correlated and share a certain brain mechanism. According to the speculative theoretical framework in [53], the visual system is assumed to be composed of the early visual processing and visual memory modules. Here, the visual memory consists of many natural scene templates and the perception or cognition task can be achieved by retrieving the matched pattern for the query image.

From the application perspective, we simulate this visual memory retrieval with a label transfer procedure, which transfers the subjective quality labels (e.g., DMOS or MOS) from

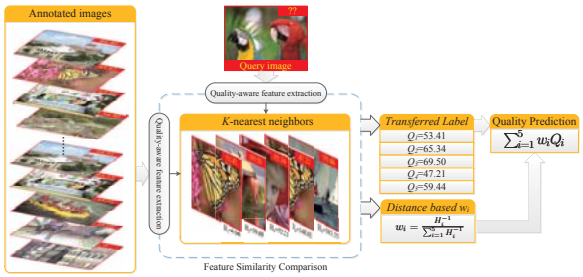


Fig. 9. Diagram of the distortion-specific label transfer for JP2K. The DMOS label of each annotated image is marked in its top-right corner. $H_i$ denotes the feature distance between the query image and its $i$th nearest neighbor.

the annotated images to the query image. It is based on the assumption that the images with similar features should share similar perceptual qualities. An instance of the distortion-specific label transfer for the JP2K is shown in Fig. 9. Here, we first search for the query image's KNN from the annotated set. There are two outputs in this stage, i.e., the transferred DMOS labels $Q_i$ and the distance based weight $w_i$. Then, we can obtain the predicted quality by integrating $Q_i$ and $w_i$. This label transfer method could adaptively update $w_i$ for each test image, which works like piecewise regression and improves the robustness of the regression model [54]. Following the two-step scheme in [16], we design the distortion-specific label transfer channel for each distortion type.

Firstly, we divide the annotated images into distortion-specific subsets, which are used for different label transfer channels, respectively. We identify the query image's distortion type with the off-line trained SVM classifier [55], whose input is the single-channel LBP feature and the outputs are the query image's probabilities of belonging to each distortion type. To prevent over-fitting, cross validation is employed to determine the classifier's parameters [56], [57].

Secondly, the distortion-specific label transfer is separately implemented in each label transfer channel. We search for the query image's KNN in the distortion-specific image subset and the KNN's labels are transferred to the query image. Then, the weighted average of the received labels is used as the predicted quality score in each label transfer channel.

Let $\mathcal{F}_i$ denote the feature vector set of the $i$th query image, where $\mathcal{F}_i = \{F_i^1, \cdots, F_i^{N_F}\}$ and $N_F$ is the number of the feature vectors. Let $\widetilde{\mathcal{F}}_j^m$ denote the feature vector set of the $j$th reference sample in the annotated image subset with the $m$th distortion type, where $\widetilde{\mathcal{F}}_j^m = \{\widetilde{F}_j^{m,1}, \cdots, \widetilde{F}_j^{m,N_F}\}$. As discussed in [58], [59], the product combination from multiple smaller classifiers could achieve the optimal classification performance for the independent training data. Thus, we use the product fusion to combine all feature similarities. We define the distance $H_{m,j}$ between $\mathcal{F}_i$ and $\widetilde{\mathcal{F}}_j^m$ as the product of the chi-square distance for each pair of the feature vectors

$$\begin{aligned} H_{m,j} &= \prod_{k=1}^{N_F} h(F_i^k, \widetilde{F}_j^{m,k}) \\ h(F_i^k, \widetilde{F}_j^{m,k}) &= \sum_{t=1}^{N_k} \frac{\left(F_i^k(t) - \widetilde{F}_j^{m,k}(t)\right)^2}{F_i^k(t) + \widetilde{F}_j^{m,k}(t)} \end{aligned} \tag{15}$$

where $F_i^k(t)$ and $\widetilde{F}_j^{m,k}(t)$ denote the $t$th element of $F_i^k$ and $\widetilde{F}_j^{m,k}$, $N_k$ is the dimension of the $k$th feature vector.

Based on our experimental study, we select the top five nearest neighbors of the query image from the current annotated image subset in terms of $H_{m,j}$, which achieves good quality prediction accuracy at low complexity. Then, a distance-based weighting scheme is used for the KNN's labels (i.e., DMOS) to predict the subjective quality in current label transfer channel. Here, a larger weight is assigned to the label which has smaller feature distance. The normalized weight $w_{m,j}$ for the $j$th selected neighbor image can be defined as

$$w_{m,j} = H_{m,j}^{-1} / \sum_{j=1}^{5} H_{m,j}^{-1} \tag{16}$$

The predicted quality of the $m$th label transfer channel is

$$Q_m = \sum_{j=1}^{5} w_{m,j} \cdot DMOS_j \tag{17}$$

By assigning larger weight to the quality index which has more similar distortion types with the query image, we can obtain the final predicted perceptual quality, i.e.,

$$Q = \sum_{m=1}^{M} p_m \cdot Q_m \tag{18}$$

where $p_m$ is the query image's probability of belonging to the $m$th distortion type, $M$ is the number of the distortion types.

## IV. Experimental Results

### A. Protocol

We test the proposed method on the LIVE II [29], TID2008 [30] and CSIQ [31] databases. The MATLAB code of our method has been released online [1]. The consistency experiment is conducted on the LIVE II database, which contains five distortion types, i.e., JP2K, JPEG, additive white noise (WN), Gaussian blur (Blur) and fast fading (FF). Similar to [14]–[16], a cross validation is implemented by randomly splitting the LIVE II database into two non-overlapped sets. We use 23 of 29 reference images and their associated distorted images as the training set. The remaining images make up the test set.

The training set is used to learn the distortion-type classifier and construct the annotated image set. Here, we conduct the random splitting evaluation 100 times. The median values of the indices across the 100 trials are used for verification. Four measures are adopted to compare different BIQA approaches, i.e., the Pearson's linear correlation coefficient (PLCC), the Spearman's rank ordered correlation coefficient (SROCC), the root-mean-square error (RMSE) and mean absolute error (MAE) between the predicted quality $Q$ and the DMOS.

### B. Feature Analysis

Since the discriminatory abilities of different features vary for different distortion types, we first investigate each feature's performance. Each candidate feature is separately used to compute the similarity between the query image and the annotated

[1] http://ivipc.uestc.edu.cn/wqb/projects/TCLT-release.zip

TABLE III
THE PERCEPTION CONSISTENCY PERFORMANCE OF EACH FEATURE

| | JP2K | JPEG | WN | Blur | FF | All | Dimension |
|---|---|---|---|---|---|---|---|
| $\mathcal{P}$ | 0.8663 | **0.8959** | 0.9451 | 0.8988 | 0.8178 | **0.8957** | 153 |
| $\mathcal{E}$ | 0.8398 | 0.8708 | 0.9789 | 0.9179 | **0.8365** | 0.8929 | 42 |
| $\mathcal{D}$ | 0.8116 | 0.8785 | **0.9818** | 0.8997 | 0.8329 | 0.8830 | 39 |
| $\hat{\mathcal{E}}$ | 0.8429 | 0.8471 | 0.9804 | **0.9299** | 0.8289 | 0.8791 | 36 |
| $\hat{\mathcal{D}}$ | 0.8524 | 0.8346 | 0.9135 | 0.9250 | 0.8440 | 0.8748 | 27 |
| LBP | **0.8680** | 0.8569 | 0.9680 | 0.9239 | 0.8118 | 0.8878 | 4116 |

TABLE IV
EACH FEATURE'S CONTRIBUTION FOR DIFFERENT DISTORTION SPECIFIC LABEL TRANSFER CHANNELS

| | DCT | | | Wavelet | | Spatial |
|---|---|---|---|---|---|---|
| | $\mathcal{P}$ | $\mathcal{E}$ | $\mathcal{D}$ | $\hat{\mathcal{E}}$ | $\hat{\mathcal{D}}$ | LBP |
| JP2K | **6.5919** | 2.1120 | 2.0308 | **5.1754** | **3.1481** | **2.2166** |
| JPEG | **4.0333** | 2.8089 | **3.8354** | **8.0938** | **3.0647** | **4.2231** |
| WN | 3.0366 | **5.5851** | 3.9220 | **4.4875** | **5.5007** | **4.2525** |
| Blur | 2.5583 | 2.9053 | **5.0398** | **6.7952** | **3.3566** | **3.5072** |
| FF | **4.4353** | 2.0834 | 1.9222 | **4.2192** | **2.8536** | **3.3435** |

reference sample across all distortion types. Here, we only use the data from the training set of the LIVE II database. Similar to Section IV-**A**, we divide these training images into the content non-overlapped annotation set and validation set, which contains 60% and 20% samples, respectively. The median SROCC of the validation set over 100 train-test trials are reported in Table III, where the optimal results in each row are labeled in boldface and the dimension of each proposed feature is listed in the last column.

It is seen that the SROCC values of the proposed features are all larger than 0.8 under different distortion types. Meanwhile, no single feature performs best across all distortion types. Thus, it is natural to select different feature combinations for each distortion-specific label transfer channel.

Let $\rho_{m,n}^k$ denote the SROCC obtained from the label transfer of the $k$th feature, where the query image belongs to the $m$th distortion type and the annotated image subset possesses the $n$th distortion type. Let $\sigma_n^k$ denote the standard derivation of the SROCC for the $k$th feature in the $n$th distortion-specific label transfer channel. Then, we can get

$$\begin{aligned}(\sigma_n^k)^2 &= \frac{1}{M}\sum_{m=1}^{M}(\rho_{m,n}^k - \mu_n^k)^2 \\ \mu_n^k &= \frac{1}{M}\sum_{m=1}^{M}\rho_{m,n}^k\end{aligned} \tag{19}$$

By considering the classification accuracy, we represent the $k$th feature contribution for the query images with the $m$th distortion type as $I_m^k$, i.e.,

$$\begin{aligned}I_m^k &= \sum_{n=1}^{M}\frac{\rho_{m,n}^k \cdot sgn(n)}{\sigma_n^k} \\ sgn(n) &= \begin{cases} a_n & n = m \\ 1 - a_n & n \neq m \end{cases}\end{aligned} \tag{20}$$

where $a_n$ is the $n$th distortion type's classification accuracy.

From (20), we know that only the feature which produces better correlation performance with DMOS (i.e., higher SROCC) and stronger robustness across different distortion types (i.e., smaller SROCC standard deviation) can bring greater contribution to current label transfer channel. Table IV shows the $I_m^k$ values, where a higher value in each row means a bigger contribution for the corresponding distortion type. For each distortion type, we select some specific features with the top $I_m^k$ values in each row of Table IV. The number of selected features is determined by cross validation, which achieves the highest median SROCC in the validation set. For clarity, the selected features are labeled by the boldface in Table IV. Meanwhile, we summarize the feature combination information for each distortion-specific label transfer channel in Table V, where the dimensions of the combined features are listed in the last column.

TABLE V
FEATURE COMBINATIONS FOR DIFFERENT DISTORTION SPECIFIC LABEL TRANSFER CHANNELS

| Feature combination ID | Distortion type | Selected features | Dimension |
|---|---|---|---|
| 1 | JP2K | $\mathcal{P},\hat{\mathcal{E}},\hat{\mathcal{D}}$,LBP | 4312 |
| 2 | JPEG | $\mathcal{P},\mathcal{D},\hat{\mathcal{E}},\hat{\mathcal{D}}$,LBP | 4351 |
| 3 | WN | $\mathcal{E},\hat{\mathcal{E}},\hat{\mathcal{D}}$,LBP | 4201 |
| 4 | Blur | $\mathcal{D},\hat{\mathcal{E}},\hat{\mathcal{D}}$,LBP | 4198 |
| 5 | FF | $\mathcal{P},\hat{\mathcal{E}},\hat{\mathcal{D}}$,LBP | 4312 |

### C. Consistency Experiment

Our method has two characteristics that guarantee high consistency with human perception, i.e., multi-channel features fusion and distortion-specific label transfer. To separately evaluate them, we implement our method with four combinations: single-channel feature + universal distortion label transfer (named as $\overline{\text{TCLT}}$-Gray); multi-channel features fusion + distortion specific label transfer (named as $\overline{\text{TCLT}}$-YCbCr); single-channel feature + distortion specific label transfer (named as TCLT-Gray); multi-channel features fusion + distortion specific label transfer (named as TCLT-YCbCr). The single-channel features are extracted from the gray image. The universal distortion label transfer doesn't identify the distortion type, and evaluates the query image with the weighted average of its KNN's labels searched from all reference images. In measuring two images' similarity, the universal distortion label transfer would combine all proposed features.

Here, we compare our method with some FR-IQA (e.g., PSNR, SSIM [7] and VIF [8]) and BIQA (e.g., BIQI [19], pLSA [60], BLINDS [14], DIIVINE [16], BLINDS-II [15], NIQE [17], NSS-TS [61] and BRISQUE [62]) algorithms.

The scatter plots for the four versions of our method are shown in Fig. 10. It can be seen that the predicted quality $Q$ shows a nearly linear relationship with DMOS. For all of $\overline{\text{TCLT}}$-Gray, $\overline{\text{TCLT}}$-YCbCr, TCLT-Gray and TCLT-YCbCr, the plots are closely distributed around the linear correlated line DMOS=$Q$. It demonstrates that all of our methods can achieve high consistency with the human perception. Meanwhile, some outliers also can be found in Fig. 10, which are far from the linear correlation line. In Fig. 10 (a), the prediction error of the JP2K version of *stream* is up to 25. In Fig. 10 (b), the prediction errors for the JP2K and FF versions of *paintedhouse* are 24 and 19, respectively. In Fig. 10 (c), the prediction error of the JP2K version of *coinsinfountain* is 22. In Fig. 10 (d), the prediction error for the FF version of *ocean* is 18.

The detailed consistency performances are shown in Table VI. The best BIQA metrics' PLCC and SROCC are highlighted in boldface under each distortion type. It can be seen

TABLE VI
MEDIAN PLCC, SROCC, RMSE AND MAE ACROSS 100 TRAIN-TEST TRIALS ON THE LIVE II IQA DATABASE

| Distortion | | JP2K | | | | JPEG | | | |
|---|---|---|---|---|---|---|---|---|---|
| Metric | Type | PLCC | SROCC | RMSE | MAE | PLCC | SROCC | RMSE | MAE |
| PSNR | FR | 0.896 | 0.890 | 7.187 | 5.528 | 0.860 | 0.841 | 8.170 | 6.380 |
| SSIM | FR | 0.937 | 0.932 | 5.671 | 4.433 | 0.928 | 0.903 | 5.947 | 4.485 |
| VIF | FR | 0.962 | 0.953 | 4.449 | 3.445 | 0.943 | 0.913 | 5.321 | 3.807 |
| pLSA | Blind | 0.87 | 0.85 | -- | -- | 0.90 | 0.88 | -- | -- |
| BIQI | Blind | 0.750 | 0.736 | 16.540 | -- | 0.630 | 0.591 | 24.580 | -- |
| BLINDS | Blind | 0.807 | 0.805 | 14.780 | -- | 0.597 | 0.552 | 25.320 | -- |
| DIIVINE | Blind | 0.922 | 0.913 | 9.660 | -- | 0.921 | 0.910 | 12.250 | -- |
| BLINDS-II | Blind | **0.963** | **0.951** | -- | -- | **0.979** | 0.942 | -- | -- |
| BRISQUE | Blind | 0.923 | 0.914 | -- | -- | 0.974 | **0.965** | -- | -- |
| NIQE | Blind | 0.937 | 0.917 | -- | -- | 0.956 | 0.938 | -- | -- |
| NSS-TS | Blind | 0.947 | 0.931 | 5.792 | 7.169 | 0.933 | 0.915 | 6.333 | 7.912 |
| $\overline{\text{TCLT}}$-Gray | Blind | 0.865 | 0.862 | 8.654 | 6.551 | 0.933 | 0.910 | 6.005 | 4.236 |
| TCLT-Gray | Blind | 0.846 | 0.839 | 9.067 | 7.000 | 0.929 | 0.912 | 6.165 | 4.424 |
| $\overline{\text{TCLT}}$-YCbCr | Blind | 0.893 | 0.889 | 7.834 | 6.171 | 0.948 | 0.932 | 5.340 | 4.023 |
| TCLT-YCbCr | Blind | 0.902 | 0.898 | 7.721 | 6.199 | 0.946 | 0.923 | 5.501 | 4.425 |
| Distortion | | WN | | | | Blur | | | |
| Metric | Type | PLCC | SROCC | RMSE | MAE | PLCC | SROCC | RMSE | MAE |
| PSNR | FR | 0.986 | 0.985 | 2.680 | 2.164 | 0.783 | 0.782 | 9.772 | 7.743 |
| SSIM | FR | 0.970 | 0.963 | 3.916 | 3.257 | 0.874 | 0.894 | 7.639 | 5.760 |
| VIF | FR | 0.984 | 0.986 | 2.851 | 2.304 | 0.974 | 0.973 | 3.533 | 2.818 |
| pLSA | Blind | 0.87 | 0.80 | -- | -- | 0.88 | 0.87 | -- | -- |
| BIQI | Blind | 0.968 | 0.958 | 6.930 | -- | 0.800 | 0.778 | 11.100 | -- |
| BLINDS | Blind | 0.914 | 0.890 | 11.270 | -- | 0.870 | 0.834 | 9.080 | -- |
| DIIVINE | Blind | 0.988 | **0.984** | 4.310 | -- | 0.923 | 0.921 | 7.070 | -- |
| BLINDS-II | Blind | 0.985 | 0.978 | -- | -- | 0.948 | 0.944 | -- | -- |
| BRISQUE | Blind | 0.985 | 0.979 | -- | -- | 0.951 | **0.951** | -- | -- |
| NIQE | Blind | 0.977 | 0.966 | -- | -- | 0.953 | 0.934 | -- | -- |
| NSS-TS | Blind | 0.963 | 0.971 | 4.464 | 6.018 | 0.950 | 0.939 | 5.481 | 6.863 |
| $\overline{\text{TCLT}}$-Gray | Blind | 0.989 | 0.980 | 2.571 | 2.080 | 0.941 | 0.928 | 5.778 | 4.576 |
| TCLT-Gray | Blind | 0.989 | 0.980 | 2.679 | 2.205 | **0.955** | 0.947 | 5.085 | 3.880 |
| $\overline{\text{TCLT}}$-YCbCr | Blind | 0.988 | 0.976 | 2.638 | 2.123 | 0.954 | 0.941 | 5.106 | 4.050 |
| TCLT-YCbCr | Blind | **0.989** | 0.979 | 2.683 | 2.166 | 0.954 | 0.940 | 5.157 | 4.057 |
| Distortion | | FF | | | | Entire database | | | |
| Metric | Type | PLCC | SROCC | RMSE | MAE | PLCC | SROCC | RMSE | MAE |
| PSNR | FR | 0.890 | 0.890 | 7.516 | 5.800 | 0.824 | 0.820 | 9.124 | 7.325 |
| SSIM | FR | 0.943 | 0.941 | 5.485 | 4.297 | 0.863 | 0.851 | 8.126 | 6.275 |
| VIF | FR | 0.962 | 0.965 | 4.502 | 3.547 | 0.950 | 0.953 | 5.024 | 3.887 |
| pLSA | Blind | 0.84 | 0.77 | -- | -- | 0.79 | 0.80 | -- | -- |
| BIQI | Blind | 0.722 | 0.700 | 19.480 | -- | 0.740 | 0.726 | 18.360 | -- |
| BLINDS | Blind | 0.743 | 0.678 | 18.620 | -- | 0.680 | 0.663 | 20.010 | -- |
| DIIVINE | Blind | 0.888 | 0.863 | 12.930 | -- | 0.917 | 0.916 | 10.900 | -- |
| BLINDS-II | Blind | **0.944** | 0.927 | -- | -- | 0.923 | 0.920 | -- | -- |
| BRISQUE | Blind | 0.903 | 0.877 | -- | -- | **0.942** | **0.940** | -- | -- |
| NIQE | Blind | 0.913 | 0.859 | -- | -- | 0.915 | 0.914 | -- | -- |
| NSS-TS | Blind | 0.942 | **0.935** | 5.232 | 7.070 | 0.926 | 0.930 | 5.131 | 6.803 |
| $\overline{\text{TCLT}}$-Gray | Blind | 0.878 | 0.835 | 8.362 | 6.003 | 0.915 | 0.910 | 6.712 | 4.704 |
| TCLT-Gray | Blind | 0.894 | 0.861 | 7.842 | 5.933 | 0.917 | 0.916 | 6.612 | 4.789 |
| $\overline{\text{TCLT}}$-YCbCr | Blind | 0.898 | 0.872 | 7.571 | 5.717 | 0.927 | 0.925 | 6.268 | 4.494 |
| TCLT-YCbCr | Blind | 0.923 | 0.903 | 6.964 | 5.160 | 0.935 | 0.934 | 5.938 | 4.326 |

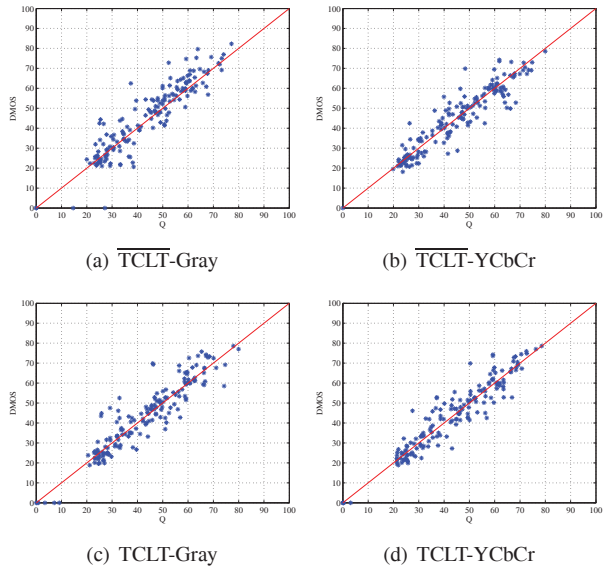


(a) $\overline{\text{TCLT}}$-Gray (b) $\overline{\text{TCLT}}$-YCbCr

(c) TCLT-Gray (d) TCLT-YCbCr

Fig. 10. The scatter plots of the predicted quality index $Q$ vs. the DMOS. The x-axis is the predicted quality index $Q$ and the y-axis is the DMOS value. The red line represents the ideal linear correlated line.

that our predicted qualities are highly consistent with the human perception across different distortion types. For Blur, the TCLT-Gray achieves the best PLCC (0.955) and the sub-optimal SROCC (0.947) result. For WN, all the $\overline{\text{TCLT}}$-Gray, TCLT-Gray and TCLT-YCbCr achieve the best performance in terms of PLCC (0.989). Both of the $\overline{\text{TCLT}}$-Gray and TCLT-Gray obtain a suboptimal SROCC (0.980) result, which are

TABLE VII
RESULTS OF THE ONESIDED T-TEST PERFORMED BETWEEN THE SROCC VALUES OBTAINED FROM FOUR VERSIONS OF THE PROPOSED METHOD. A VALUE OF "1"/"0"/"-1" INDICATES THE ROW ALGORITHM IS STATISTICALLY SUPERIOR/EQUIVALENT/INFERIOR TO THE COLUMN ALGORITHM

| | $\overline{\text{TCLT}}$-Gray | TCLT-Gray | $\overline{\text{TCLT}}$-YCbCr | TCLT-YCbCr |
|---|---|---|---|---|
| $\overline{\text{TCLT}}$-Gray | 0 | -1 | -1 | -1 |
| TCLT-Gray | 1 | 0 | -1 | -1 |
| $\overline{\text{TCLT}}$-YCbCr | 1 | 1 | 0 | -1 |
| TCLT-YCbCr | 1 | 1 | 1 | 0 |

close to the best DIIVINE result (SROCC=0.984). For the JPEG and FF, the $\overline{\text{TCLT}}$-YCbCr and TCLT-YCbCr achieve the fourth best performance, respectively. For JP2K, the PLCC of the TCLT-YCbCr is still more than 0.9.

For the general purpose BIQA, the predicted quality should work well for all distortion types. Here, our TCLT-YCbCr method achieves the second best result (SROCC=0.934) in the entire database test, which is very close to the state-of-the-art BRISQUE metric (SROCC=0.940). A onesided *t-test* [63] is also executed on the SROCC of the proposed method and BRISQUE across 100 train-test trails. The reported result shows that the four versions of our proposed method are statistically inferior to the BRISQUE in this test.

In addition, the entire database test verifies that the multi-channel features fusion and distortion-specific label transfer are both valid in improving the BIQA performance. Firstly, the multi-channel fusion features capture more comprehensive visual perception properties than the single-channel features. Thus, it is found that $\overline{\text{TCLT}}$-YCbCr (SROCC=0.925) outperforms $\overline{\text{TCLT}}$-Gray (SROCC=0.910) and TCLT-YCbCr

TABLE VIII
STANDARD DERIVATION OF THE $\overline{\text{TCLT}}$-GRAY'S AND $\overline{\text{TCLT}}$-YCBCR'S PERFORMANCES ACROSS 100 TRAIN-TEST TRIALS ON THE LIVE II IQA DATABASE

| | $\overline{\text{TCLT}}$-Gray | | | | $\overline{\text{TCLT}}$-YCbCr | | | |
|---|---|---|---|---|---|---|---|---|
| | PLCC | SROCC | RMSE | MAE | PLCC | SROCC | RMSE | MAE |
| JP2K | 0.040 | 0.045 | 1.251 | 1.038 | 0.037 | 0.042 | 1.291 | 1.062 |
| JPEG | 0.020 | 0.032 | 0.945 | 0.727 | 0.017 | 0.026 | 0.937 | 0.631 |
| WN | 0.003 | 0.007 | 0.364 | 0.310 | 0.003 | 0.008 | 0.367 | 0.324 |
| Blur | 0.029 | 0.036 | 0.949 | 0.826 | 0.021 | 0.026 | 0.937 | 0.790 |
| FF | 0.085 | 0.090 | 2.327 | 1.465 | 0.095 | 0.104 | 2.767 | 1.547 |
| All | 0.023 | 0.021 | 0.866 | 0.539 | 0.023 | 0.023 | 0.912 | 0.467 |

TABLE IX
STANDARD DERIVATION OF THE TCLT-GRAY'S AND TCLT-YCBCR'S PERFORMANCES ACROSS 100 TRAIN-TEST TRIALS ON THE LIVE II IQA DATABASE

| | TCLT-Gray | | | | TCLT-YCbCr | | | |
|---|---|---|---|---|---|---|---|---|
| | PLCC | SROCC | RMSE | MAE | PLCC | SROCC | RMSE | MAE |
| JP2K | 0.046 | 0.052 | 1.496 | 1.162 | 0.038 | 0.038 | 1.329 | 1.014 |
| JPEG | 0.021 | 0.034 | 0.948 | 0.727 | 0.016 | 0.027 | 0.910 | 0.653 |
| WN | 0.003 | 0.008 | 0.373 | 0.346 | 0.003 | 0.008 | 0.385 | 0.340 |
| Blur | 0.019 | 0.021 | 0.858 | 0.709 | 0.020 | 0.025 | 0.919 | 0.745 |
| FF | 0.079 | 0.074 | 2.309 | 1.447 | 0.060 | 0.058 | 2.324 | 1.443 |
| All | 0.023 | 0.022 | 0.947 | 0.554 | 0.020 | 0.019 | 0.874 | 0.478 |

(SROCC=0.934) outperforms TCLT-Gray (SROCC=0.916). Secondly, the distortion-specific label transfer provides refined reference image subset, which helps the query image to find more accurate references than the universal distortion label transfer. So, it is seen that TCLT-Gray outperforms $\overline{\text{TCLT}}$-Gray and TCLT-YCbCr outperforms $\overline{\text{TCLT}}$-YCbCr. The TCLT-YCbCr, which combines both of the aforementioned traits, performs best in all versions of our method. To evaluate the statistical significance of the difference between four versions of our method, we perform the onesided *t-test* [63] on their SROCC across 100 train-test trials. As shown in Table VII, we can find that TCLT-YCbCr still consistently outperforms the other versions of the proposed method.

In Tables VIII and IX, we further show the standard derivations of the four indices for the proposed methods across 100 train-test trials. It can be seen that the standard derivations of the four indices are very small for all the proposed methods. It demonstrates that the performance variations of the proposed methods are insignificant in the 100 trials.

### D. Classification accuracy

The distortion-specific label transfer assumes that the reference subset, which has the same distortion type with the query image, improves the accuracy of the label transfer. Thus, the classification accuracy plays an important role in our TCLT-YCbCr method. Here, we investigate the median accuracies of our distortion type classification across 100 train-test trials. As shown in Table X, it is seen that our classification accuracy is significantly superior to the DIIVINE for every distortion type and the entire database. Especially for JPEG and WN, our classification accuracies are both up to 100%.

In Table XI, we also show the standard derivations of the classification accuracies across 100 train-test trials. It is seen that the standard derivations of our distortion type classification are very small, which demonstrates that our classification performance varies very slightly in the 100 trials.

### E. Database independency

To verify that the proposed method is independent of the dataset, we further test our method on the subsets of TID2008

TABLE X
MEDIAN CLASSIFICATION ACCURACY (%) ACROSS 100 TRAIN-TEST TRIALS ON THE LIVE II IQA DATABASE

| | JP2K | JPEG | WN | Blur | FF | All |
|---|---|---|---|---|---|---|
| DIIVINE | 80.00 | 81.10 | 100.00 | 90.00 | 73.30 | 83.75 |
| TCLT | 85.71 | 100.00 | 100.00 | 96.67 | 80.00 | 90.85 |

TABLE XI
STANDARD DERIVATION OF THE CLASSIFICATION ACCURACY ACROSS 100 TRAIN-TEST TRIALS ON THE LIVE II IQA DATABASE

| | JP2K | JPEG | WN | Blur | FF | All |
|---|---|---|---|---|---|---|
| TCLT | 8.56 | 3.38 | 1.54 | 2.95 | 10.91 | 2.62 |

[30] and CSIQ [31] databases. The entire LIVE II database is used as the train set. Four types of "known" distortions in the train set are selected from the TID2008 and CSIQ to construct the test set, i.e., JP2K, JPEG, WN and Blur.

The detailed SROCC performances on TID2008 and CSIQ are presented in Table XII and Table XIII, respectively. For comparison, we also show the performances of two FR metrics PSNR and SSIM in Tables XII and XIII. The performances of three BIQA metrics DIIVINE, BLINDS-II and BRISQUE are also involved here, where the best BIQA metrics are highlighted by boldface. It is clear that all the four versions of the proposed method still achieve highly consistent evaluation with the human perception. In addition, due to the contributions of multi-channel features fusion and distortion-specific label transfer, the TCLT-YCbCr also performs best in all the four proposed methods for both TID2008 and CSIQ databases, which is consistent with the result in LIVE II test.

Based on the experimental results here, we find that the four versions of the proposed method perform similarly on each database. If only a complete training set is properly constructed, the proposed four methods can accurately predict the perceptual quality of a degraded image.

### F. Impact of the neighbor number

Here, we investigate the performance variation of the proposed method under different $K$, whose value ranges from 1 to 100 with an interval of 5. The investigation is implemented on the LIVE II database. Except for the $K$, all the other settings are the same like the Section IV-**C**. The median values of the RMSE across 100 train-test trials are reported in Fig. 11.

It is seen that when we change $K$ from 1 to 20, the RMSE would significantly drop from 7.13 to 5.46. That is, a larger number of neighbors could avoid a large prediction error, which is caused by mistaking the neighbors' perceptual similarities. Then, the RMSE slowly increases and converges to 5.62 as $K$ changes from 20 to 100. Here, too many neighbors would increase the model bias for introducing the dissimilar images. Since we employ the distance based weight scheme, the predicted quality sores would not tend to the mean of the annotated database like the arithmetic averaging [64]. This can be found from Fig. 11, where our RMSE does not significantly increase as $K$ increases to 100.

To evaluate the performance of our TCLT-YCbCr with 20 neighbors, we repeat the experiments on Sections IV-**C** and IV-**E**. The SROCC results on LIVE II, TID2008 and CSIQ databases are reported in Table XIV, where the best results under each distortion type are highlighted by boldface. It is

TABLE XII
SROCC BETWEEN THE PREDICTED QUALITY INDEX AND MOS ON THE "KNOWN" SUBSETS OF THE TID2008 DATABASE

| Metric | Type | JP2K | JPEG | WN | Blur | All |
|---|---|---|---|---|---|---|
| PSNR | FR | 0.825 | 0.876 | 0.918 | 0.934 | 0.870 |
| SSIM | FR | 0.963 | 0.935 | 0.817 | 0.960 | 0.902 |
| DIIVINE | Blind | 0.924 | 0.866 | **0.851** | 0.862 | 0.889 |
| BLINDS-II | Blind | 0.915 | 0.889 | 0.696 | 0.857 | 0.854 |
| BRISQUE | Blind | 0.832 | **0.924** | 0.829 | 0.881 | **0.896** |
| TCLT-Gray | Blind | 0.880 | 0.783 | 0.794 | 0.870 | 0.845 |
| TCLT-Gray | Blind | 0.863 | 0.760 | 0.779 | 0.849 | 0.843 |
| TCLT-YCbCr | Blind | **0.925** | 0.874 | 0.802 | **0.879** | 0.872 |
| TCLT-YCbCr | Blind | 0.890 | 0.895 | 0.830 | 0.872 | 0.877 |

TABLE XIII
SROCC BETWEEN THE PREDICTED QUALITY INDEX AND DMOS ON THE "KNOWN" SUBSETS OF THE CSIQ DATABASE

| Metric | Type | JP2K | JPEG | WN | Blur | All |
|---|---|---|---|---|---|---|
| PSNR | FR | 0.936 | 0.888 | 0.936 | 0.925 | 0.921 |
| SSIM | FR | 0.958 | 0.944 | 0.898 | 0.958 | 0.926 |
| DIIVINE | Blind | 0.830 | 0.704 | 0.797 | 0.871 | 0.828 |
| BLINDS-II | Blind | 0.884 | 0.881 | 0.886 | 0.870 | 0.873 |
| BRISQUE | Blind | 0.857 | 0.877 | 0.926 | 0.874 | 0.881 |
| TCLT-Gray | Blind | 0.868 | 0.864 | 0.878 | 0.874 | 0.858 |
| TCLT-Gray | Blind | 0.876 | 0.890 | 0.883 | 0.895 | 0.878 |
| TCLT-YCbCr | Blind | 0.894 | 0.898 | **0.928** | **0.896** | 0.886 |
| TCLT-YCbCr | Blind | **0.896** | **0.907** | 0.908 | 0.882 | **0.891** |

interesting to see that our method outperforms all the other BIQA metrics in the LIVE II and CSIQ databases. In the TID database, our method still works well and achieves a high consistency with human perception. Since the results in LIVE II are obtained from 100 train-test trials, we further perform a onesided *t-test* to evaluate the statistical significance of the difference between different BIQA methods. The reported result confirms that when $K$ is set to 20, our TCLT-YCbCr is statistically superior to all of the DIIVINE, BLINDS-II and BRISQUE metrics on the LIVE II database.

### G. Comparison among different color space

Here, we further investigate the performance of our multi-channel features under different color spaces, which include the RGB, Lab and YCbCr. We repeat the experiments in Sections IV-**C** and IV-**E**. For each candidate color space, the SROCC values on LIVE II, TID2008, CSIQ and their average results across the three databases are reported in Fig. 12.

It is seen that the performance of the RGB is inferior to the Lab and YCbCr on the three databases. There are two possible reasons accounting for this result: Firstly, both the Lab and YCbCr represent the color image with one luma and two chroma components. Since the chroma components are insensitive to the illumination change, it could improve the discriminative power of the features in describing the natural scene [65]. Secondly, by transforming from the RGB to the Lab/YCbCr, the high-frequency image content is preserved in the luma component and the smooth information is stored in the chroma components. Then, the statistics on Lab/YCbCr can capture more comprehensive intrascale correlations from different color channels [66].

In addition, it can be seen that the Lab and YCbCr achieve similar performance. As shown in Fig. 12, the YCbCr slightly outperforms the Lab in LIVE II. In TID, the Lab performs better than the YCbCr. For CSIQ, the YCbCr achieves the same SROCC result as the Lab. On average, the Lab and YCbCr also achieve the same performance across these three databases, whose average SROCC are both 0.901.

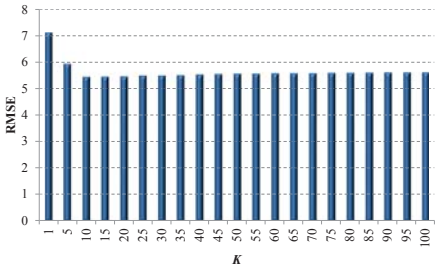


Fig. 11. The median RMSE variation of TCLT-YCbCr under different $K$.

TABLE XIV
THE PERFORMANCE OF THE TCLT-YCBCR METHOD WITH $K$=20

| Database | Metric | JP2K | JPEG | WN | Blur | FF | All |
|---|---|---|---|---|---|---|---|
| LIVE II | DIIVINE | 0.913 | 0.910 | **0.984** | 0.921 | 0.863 | 0.916 |
| | BLINDS-II | **0.951** | 0.942 | 0.978 | 0.944 | **0.927** | 0.920 |
| | BRIQUSE | 0.914 | **0.965** | 0.979 | 0.951 | 0.877 | 0.940 |
| | TCLT-YCbCr | 0.917 | 0.925 | 0.981 | **0.953** | 0.921 | **0.944** |
| TID2008 | DIIVINE | 0.924 | 0.866 | **0.851** | 0.862 | -- | 0.889 |
| | BLINDS-II | 0.915 | 0.889 | 0.696 | 0.857 | -- | 0.854 |
| | BRIQUSE | 0.832 | **0.924** | 0.829 | **0.881** | -- | **0.896** |
| | TCLT-YCbCr | **0.930** | 0.878 | 0.839 | 0.864 | -- | 0.879 |
| CSIQ | DIIVINE | 0.830 | 0.704 | 0.797 | 0.871 | -- | 0.828 |
| | BLINDS-II | 0.884 | 0.881 | 0.886 | 0.870 | -- | 0.873 |
| | BRIQUSE | 0.857 | 0.877 | **0.926** | 0.874 | -- | 0.881 |
| | TCLT-YCbCr | **0.900** | **0.915** | 0.910 | **0.898** | -- | **0.892** |

### H. Completeness of the annotated image set

Here, we further discuss the completeness of the annotated samples. For our TCLT-YCbCr method, the completeness requires that the query image could find some similar images in the annotated sample set. It should satisfy two points: 1) the annotated set should cover all available DMOS values; 2) the annotated set should contain all possible distortion types.

*1) Impact of the annotated sample size:* Here, we investigate the impact of the DMOS coverage by varying the annotated sample size. The experiment in Section IV-**C** is repeated with different train-test splits, where the percentage of train set ranges from 10% to 90%. The median SROCC variation versus the percentage of train set is reported in Fig. 13, where the results of DIIVINE, BLINDS-II and BRISQUE are also added for comparison.

It can be seen that our method outperforms all the other BIQA metrics under the train set size 10%-60%. For the train set size 70%-90%, our TCLT-YCbCr method is slightly inferior to the BRISQUE metric. When only 10% samples are used for training, our TCLT-YCbCr method can obtain a reasonable performance in the LIVE II database, whose median SROCC reaches up to 0.8668. In addition, we can also find that the SROCC of all BIQA metrics monotonically go up as the train set size increases. Because a larger training set would cover more dense DMOS values, it makes the train set more complete and facilitates the label transfer.

*2) Impact of the "unknown" distortion type:* Here, we implement the cross-database experiment to investigate the train set's completeness in terms of the distortion type. The LIVE II database is used as the annotated set. The test set is constructed with 13 "unknown" distortion types in TID2008, which are Additive noise in color components (ANC), Spatially correlated noise (SCN), Masked noise (MN), High frequency noise (HFN), Impulse noise (IN), Quantization noise (QN), Image denoising (ID), JPEG transmission errors (JPEGTE), JPEG2000 transmission errors (JP2KTE), Non eccentricity pattern noise (NEPN), Local block-wise distortions of different

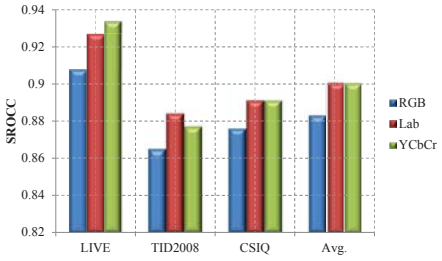


Fig. 12. The performance comparison for TCLT under different color spaces.

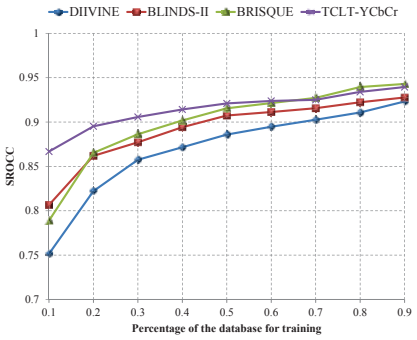


Fig. 13. The plot of median SROCC between the predicted quality index $Q$ and DMOS versus the percentage of the images used for annotated set.

intensity (LBDDI), Mean shift (MS) and Contrast change (CC). The SROCC of our methods are reported in Table XV. For comparison, the BRISQUE [62] is also tested here.

Since the test images distortion types are not present in the annotated samples, it is hard for us to implement an efficient label transfer. For SCN, QN, JPEGTE, JP2KTE, NEPN, LBDDI, MS and CSS, their SROCC are all smaller than 0.5 for the TCLT-YCbCr. However, when the "unknown" distortion types show some similar characteristics with the annotated samples, the proposed method would still work well. For example, the ANC, HFN, IN and MN are similar to the WN, and the ID is similar to Blur. Correspondingly, our TCLT-YCbCr method achieves relatively high SROCC values on these distortion types, which are all larger than 0.65. Similar results can be found for the BRISQUE. Experimental results show that the application of TCLT-YCbCr is limited to certain distortion types which are similar to the training data.

### *I. Computational analysis*

In this section, we further analyze the computational complexity of the proposed method. This investigation is conducted on the LIVE II database, whose 80% images are used for constructing the annotated reference samples. The system platform is an Intel Core 2 processor of speed 2.0 GHz, 2 GB RAM and Windows 7. The unoptimized MATLAB code is run on the MATLAB R2009b software. Here, it takes about 10 seconds to predict the quality of a 512×768 image, which includes both the feature extraction and the label transfer steps.

In order to compare the computational loads of each module, both the percentage of running time and the time complexity for each module are summarized in Table XVI. Compared with the existing BIQA metrics [15], [16], the

TABLE XV
SROCC PERFORMANCE OF TCLT-YCBCR ON THE "UNKNOWN" SUBSETS OF THE TID2008 DATABASE

| | ANC | SCN | MN | HFN | IN | QN | ID |
|---|---|---|---|---|---|---|---|
| BRISQUE | 0.713 | -0.495 | 0.583 | 0.623 | 0.582 | 0.739 | 0.570 |
| TCLT-Gray | 0.765 | 0.365 | 0.824 | 0.862 | 0.889 | 0.194 | 0.710 |
| TCLT-Gray | 0.733 | 0.490 | 0.816 | 0.863 | 0.799 | -0.253 | 0.614 |
| TCLT-YCbCr | 0.818 | 0.625 | 0.830 | 0.882 | 0.827 | 0.681 | 0.673 |
| TCLT-YCbCr | 0.771 | 0.454 | 0.817 | 0.888 | 0.736 | 0.022 | 0.690 |
| | JPEGTE | JP2KTE | NEPN | LBDDI | MS | CC | |
| BRISQUE | 0.288 | 0.260 | 0.160 | 0.165 | 0.091 | -0.052 | |
| TCLT-Gray | 0.018 | -0.127 | -0.154 | 0.014 | 0.110 | 0.008 | |
| TCLT-Gray | -0.093 | 0.374 | -0.153 | 0.139 | 0.233 | -0.128 | |
| TCLT-YCbCr | -0.180 | -0.028 | 0.128 | 0.030 | -0.069 | 0.095 | |
| TCLT-YCbCr | -0.123 | 0.171 | 0.025 | 0.219 | 0.122 | 0.314 | |

TABLE XVI
COMPUTATIONAL COMPLEXITY FOR EACH FEATURE DOMAIN. ($N$: THE NUMBER OF PIXELS IN AN IMAGE)

| Module | Percentage of Time (%) | Complexity | Note |
|---|---|---|---|
| DCT | 78.43 | $O\left(N/d^2 \log_2(N/d^2) + b \cdot N/d^2 + (2f-1)\cdot c\right)$ | $d$: block size, $b$: no. of skewness bins<br>$f$: no. of freq. bands, $c$: no. of coefficient bins |
| Wavelet | 11.74 | $O\left(N \log_2 N + (2\hat{f}-1)\cdot \hat{c}\right)$ | $\hat{f}$: no. of subbands, $\hat{c}$: no. of coefficient bins |
| Spatial | 7.73 | $O(N)$ | |
| LT | 2.09 | $O(N_r)$ | $N_r$: no. of reference images |

proposed method introduces an extra online prediction module LT. However, its complexity $O(N_r)$ is determined by the number of the annotated reference samples, which is negligible with respect to the total complexity. As shown in Table XVI, the LT module only takes 2% of running time in the proposed method.

In addition, the complexities listed in Table XVI show the upper bound of each module, which is computed in terms of the serial operation. In fact, the proposed algorithm is highly parallelizable, where the quality-aware information can be extracted from multiple domains simultaneously. Accordingly, the application of our proposed TCLT method should not suffer the limitation due to its complexity.

### *J. Discussion*

Since the proposed DCT domain features are not shift invariant, a simple translation on the image may result in significant change on the features. An alternative solution is to add the shifted images in the annotated set. In our future work, more robust features will be studied. Similar to many previous works, we assume that a single distortion is present in the image, which is consistent with the condition in existing IQA databases. In many situations, an image may be contaminated by multiple sources, which brings greater difficulty for BIQA. Until now, the BIQA for the hybrid distortion is still a challenging problem and there are few reliable hybrid distortion IQA databases. In our future work, we would make efforts to build the hybrid distortion IQA data and extend the proposed method to deal with this new problem.

## V. APPLICATION FOR IMAGE AUTO-DENOISING

To verify the efficiency of the proposed algorithm, we further investigate its performance in an image denoising application. Many representative denoising methods require some manual parameters (e.g., noise variance) to obtain good result. However, in practice, it is impractical to manually select the parameters for each test image. Here, the BIQA metric

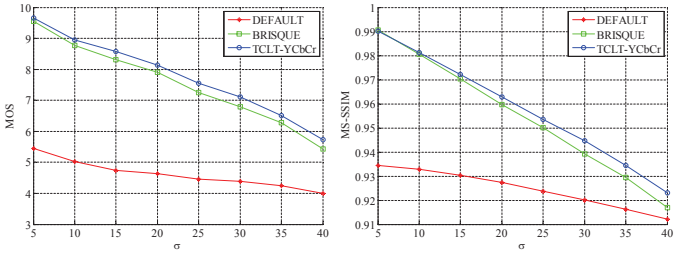


(a) MOS (b) MS-SSIM

Fig. 14. The mean quality of the denoised images at each noise level. The x-axis denotes the noise variance $\sigma$ and the y-axis denotes the quality metric. (a) the subjective metric MOS and (b) the objective metric MS-SSIM.

is quite desirable in estimating the perceptual quality of the denoised image, which could help us to automatically choose the denoising parameter.

We incorporate our TCLT-YCbCr metric into a representative color image denoising algorithm CBM3D [67], which needs the noise variance $\sigma$ as the input parameter. In our implementation, the test image is first denoised with different parameters, and then the BIQA metric is used to evaluate the perceptual quality of each denoised image. By choosing the parameter which produces the highest image quality, we can obtain a good denoising result without user intervention. Here, the LIVE II database is still used as the annotated set for our TCLT-YCbCr method. To avoid overlapping between the annotated set and the test set, we build a denoised image dataset, whose 23 original images are extracted from the CVG-UGR database (http://decsai.ugr.es/cvg/dbimagenes/). We add 8 levels of Gaussian noise to each original image, where $\sigma$ can range from 5 to 40 at an interval of 5.

In the testing stage, the denoising results obtained by the default parameter [67] are used as the benchmark. For our method, we run the CBM3D with 50 candidate $\sigma$, which ranges from 1 to 50. Then, the denoised image which is perceived best for our proposed metric is selected as the output. For comparison, the denoising results chosen by the BRISQUE metric are also investigated here. In the subjective test, we invite 12 subjects to rate the perceptual quality for each denoised image, where the subjective score can range from 1 to 10 and a larger value denotes a better quality. Then, the mean opinion score (MOS) across 12 subjects is assigned to each denoised image. Besides the MOS, an objective metric MS-SSIM [68] is also used to measure the denoising results.

Here, we compute the mean quality of 23 denoised images at each distortion level to compare different methods. Both the subjective and objective evaluation results are shown in Fig. 14. It can be seen that the denoised image's quality could be significantly improved by selecting the parameter with the TCLT-YCbCr and BRISQUE metrics. In addition, in terms of both the MOS and MS-SSIM, the denoising results obtained from our TCLT-YCbCr are better than BRISQUE as shown in Fig. 14. In addition, we also implement the onesided *t-test* on the MOS and MS-SSIM of all denoised images. The reported result shows that our TCLT-YCbCr based denoising results are statistically superior to the BRISQUE and default methods in both the subjective and objective metrics.

## VI. Conclusion

In this paper, we propose a novel blind image quality assessment algorithm based on distortion-type classification and label transfer. Inspired by the hierarchical and trichromatic properties of human vision, we extract both the frequency and spatial-frequency features from all three YCbCr channels to describe a natural image. Then, a KNN based label transfer model is used to estimate the query image's quality. Both the validity and robustness of the proposed algorithm have been verified through the experiments on LIVE II, TID2008 and CSIQ databases. In addition, experimental results show that the application of the proposed method is limited to certain distortion types which are similar to the training data. It is still a challenging task to deal with the unknown distortion types.

In our future work, the mid-level features will be studied to simulate the more complex visual perception properties, e.g., shape selectivity, saliency, etc. In addition, a more efficient similarity metric will be studied to further improve the performance of the label transfer module.

## References

[1] Z. Wang, "Applications of objective image quality assessment methods [applications corner]," *IEEE Signal Process. Mag.*, vol. 28, no. 6, pp. 137–142, 2011.

[2] Z. Wang and A. Bovik, "Reduced- and no-reference image quality assessment," *IEEE Signal Process. Mag.*, vol. 28, no. 6, pp. 29–40, 2011.

[3] J. Jiang, K. Qiu, and G. Xiao, "A block-edge-pattern-based content descriptor in DCT domain," *IEEE Trans. Circuits Syst. Video Technol.*, vol. 18, no. 7, pp. 994–998, July 2008.

[4] P.-C. Wu and L.-G. Chen, "An efficient architecture for two-dimensional discrete wavelet transform," *IEEE Trans. Circuits Syst. Video Technol.*, vol. 11, no. 4, pp. 536–545, Apr 2001.

[5] H. Liu and I. Heynderickx, "Visual attention in objective image quality assessment: Based on eye-tracking data," *IEEE Trans. Circuits Syst. Video Technol.*, vol. 21, no. 7, pp. 971–982, July 2011.

[6] H. Li and K. N. Ngan, "A co-saliency model of image pairs," *IEEE Trans. Image Process.*, vol. 20, no. 12, pp. 3365–3375, 2011.

[7] Z. Wang, A. Bovik, H. Sheikh, and E. Simoncelli, "Image quality assessment: from error visibility to structural similarity," *IEEE Trans. Image Process.*, vol. 13, no. 4, pp. 600–612, 2004.

[8] H. Sheikh and A. Bovik, "Image information and visual quality," *IEEE Trans. Image Process.*, vol. 15, no. 2, pp. 430–444, 2006.

[9] Z. Gao and Y. Zheng, "Quality constrained compression using DWT-based image quality metric," *IEEE Trans. Circuits Syst. Video Technol.*, vol. 18, no. 7, pp. 910–922, July 2008.

[10] J. Wu, W. Lin, G. Shi, and A. Liu, "Perceptual quality metric with internal generative mechanism," *IEEE Trans. Image Process.*, vol. 22, no. 1, pp. 43–54, 2013.

[11] I. Gkioulekas, G. Evangelopoulos, and P. Maragos, "Spatial Bayesian surprise for image saliency and quality assessment," in *Proc. IEEE Int. Conf. Image Process.*, 2010, pp. 1081–1084.

[12] J. Redi, P. Gastaldo, I. Heynderickx, and R. Zunino, "Color distribution information for the reduced-reference assessment of perceived image quality," *IEEE Trans. Circuits Syst. Video Technol.*, vol. 20, no. 12, pp. 1757–1769, Dec 2010.

[13] R. Soundararajan and A. Bovik, "RRED indices: Reduced reference entropic differencing for image quality assessment," *IEEE Trans. Image Process.*, vol. 21, no. 2, pp. 517–526, 2012.

[14] M. Saad, A. Bovik, and C. Charrier, "A DCT statistics-based blind image quality index," *IEEE Signal Process. Lett.*, vol. 17, no. 6, pp. 583–586, 2010.

[15] M. Saad, A. C. Bovik, and C. Charrier, "Blind image quality assessment: A natural scene statistics approach in the DCT domain," *IEEE Trans. Image Process.*, vol. 21, no. 8, pp. 3339–3352, Aug. 2012.

[16] A. K. Moorthy and A. C. Bovik, "Blind image quality assessment: From natural scene statistics to perceptual quality," *IEEE Trans. Image Process.*, vol. 20, no. 12, pp. 3350–3364, Dec. 2011.

[17] A. Mittal, R. Soundararajan, and A. Bovik, "Making a "completely blind" image quality analyzer," *IEEE Signal Process. Lett.*, vol. 20, no. 3, pp. 209–212, March 2013.

[18] H. Tang, N. Joshi, and A. Kapoor, "Learning a blind measure of perceptual image quality," in *Proc. IEEE Conf. Comput. Vis. Pattern Recognit.*, 2011, pp. 305–312.

[19] A. Moorthy and A. Bovik, "A two-step framework for constructing blind image quality indices," *IEEE Signal Process. Lett.*, vol. 17, no. 5, pp. 513–516, 2010.

[20] C. Li, A. Bovik, and X. Wu, "Blind image quality assessment using a general regression neural network," *IEEE Trans. Neural Netw.*, vol. 22, no. 5, pp. 793–799, 2011.

[21] B. Schölkopf, A. J. Smola, R. C. Williamson, and P. L. Bartlett, "New support vector algorithms," *Neural Comput.*, vol. 12, no. 5, pp. 1207–1245, May 2000.

[22] D. F. Specht, "A general regression neural network," *IEEE Trans. Neural Netw.*, vol. 2, no. 6, pp. 568–576, Nov 1991.

[23] S. Marcelja, "Mathematical description of the responses of simple cortical cells," *J. Opt. Soc. Am.*, vol. 70, pp. 1297–1300, Nov. 1980.

[24] D. M. MacKay, "Strife over visual cortical function," *Nature*, vol. 289, no. 5794, pp. 117–118, 1981.

[25] S. G. Solomon and P. Lennie, "The machinery of colour vision," *Nature Reviews Neuroscience*, vol. 8, no. 4, pp. 276–286, 2007.

[26] Q. Wu, H. Li, K. Ngan, B. Zeng, and M. Gabbouj, "No reference image quality metric via distortion identification and multi-channel label transfer," in *Proc. of IEEE Int. Symp. on Circuits and Systems*, June 2014, pp. 530–533.

[27] N. Kruger, P. Janssen, S. Kalkan, M. Lappe, A. Leonardis, J. Piater, A. Rodriguez-Sanchez, and L. Wiskott, "Deep hierarchies in the primate visual cortex: What can we learn for computer vision?" *IEEE Trans. Pattern Anal. Mach. Intell.*, vol. 35, no. 8, pp. 1847–1871, Aug 2013.

[28] D. J. Felleman and D. C. Van Essen, "Distributed hierarchical processing in the primate cerebral cortex," *Cerebral cortex*, vol. 1, no. 1, pp. 1–47, 1991.

[29] H. R. Sheikh, Z. Wang, L. Cormack, and A. C. Bovik, *LIVE Image Quality Assessment Database Release 2*, [Online]. Available: http://live.ece.utexas.edu/research/quality.

[30] N. Ponomarenko, V. Lukin, A. Zelensky, K. Egiazarian, M. Carli, and F. Battisti, "TID2008 - a database for evaluation of full-reference visual quality assessment metrics," *Advances of Modern Radioelectronics*, vol. 10, pp. 30–45, 2009.

[31] E. C. Larson and D. M. Chandler, *Categorical image quality (CSIQ) database*, [Online]. Available: http://vision.okstate.edu/csiq.

[32] D. Gao and N. Vasconcelos, "Discriminant saliency for visual recognition from cluttered scenes." in *Adv. Neural Inform. Process. Syst.*, 2004.

[33] J. Solomon, A. Watson, and A. Ahumada, "Visibility of DCT basis functions: effects of contrast masking," in *Data Compression Conference*, Mar 1994, pp. 361–370.

[34] H. B. Barlow, "Understanding natural vision," in *Physical and biological processing of images*. Springer, 1983, pp. 2–14.

[35] C. Tu and T. Tran, "Context-based entropy coding of block transform coefficients for image compression," *IEEE Trans. Image Process.*, vol. 11, no. 11, pp. 1271–1283, Nov 2002.

[36] von Hippel and P. T., "Mean, median, and skew: Correcting a textbook rule," *Journal of Statistics Education*, vol. 13, no. 2, Jul. 2005.

[37] D. J. Field, "Relations between the statistics of natural images and the response properties of cortical cells," *J. of Opt. Soc. Am. A*, vol. 4, no. 12, pp. 2379–2394, 1987.

[38] T. M. Cover and J. A. Thomas, *Elements of Information Theory*, 2nd ed. Wiley-Interscience, 2006.

[39] M. Kristan, J. Perš, M. Perše, and S. Kovačič, "A Bayes-spectral-entropy-based measure of camera focus using a discrete cosine transform," *Pattern Recognition Letters*, vol. 27, no. 13, pp. 1431–1439, 2006.

[40] Z. He, W. Lu, W. Sun, and J. Huang, "Digital image splicing detection based on Markov features in DCT and DWT domain," *Pattern Recognition*, vol. 45, no. 12, pp. 4292 – 4299, 2012.

[41] B. D. Willmore, R. J. Prenger, and J. L. Gallant, "Neural representation of natural images in visual area V2," *Journal of Neuroscience*, vol. 30, no. 6, pp. 2102–2114, 2010.

[42] Y. Karklin and M. S. Lewicki, "Emergence of complex cell properties by learning to generalize in natural scenes," *Nature*, vol. 457, no. 7225, pp. 83–86, 2009.

[43] M. Gavish, B. Nadler, and R. R. Coifman, "Multiscale wavelets on trees, graphs and high dimensional data: Theory and applications to semi supervised learning," in *Proc. Int. Conf. on Machine Learning*, 2010, pp. 367–374.

[44] J. Liu and P. Moulin, "Information-theoretic analysis of interscale and intrascale dependencies between image wavelet coefficients," *IEEE Trans. Image Process.*, vol. 10, no. 11, pp. 1647–1658, 2001.

[45] B.-J. Kim and W. Pearlman, "An embedded wavelet video coder using three-dimensional set partitioning in hierarchical trees (SPIHT)," in *Data Compression Conference*, 1997, pp. 251–260.

[46] Y. El-Shamayleh and J. A. Movshon, "Neuronal responses to texture-defined form in macaque visual area V2," *Journal of Neuroscience*, vol. 31, no. 23, pp. 8543–8555, 2011.

[47] L. G. Appelbaum, A. R. Wade, V. Y. Vildavski, M. W. Pettet, and A. M. Norcia, "Cue-invariant networks for figure and background processing in human visual cortex," *Journal of Neuroscience*, vol. 26, no. 45, pp. 11 695–11 708, 2006.

[48] T. Ojala, M. Pietikainen, and T. Maenpaa, "Multiresolution gray-scale and rotation invariant texture classification with local binary patterns," *IEEE Trans. Pattern Anal. Mach. Intell.*, vol. 24, no. 7, pp. 971–987, 2002.

[49] A. Ford and A. Roberts, "Colour space conversions," *Westminster University, London*, vol. 1998, pp. 1–31, 1998.

[50] J. Huang and Y. Wang, "Compression of color facial images using feature correction two-stage vector quantization," *IEEE Trans. Image Process.*, vol. 8, no. 1, pp. 102–109, Jan 1999.

[51] S. Fan, T.-T. Ng, J. Herberg, B. Koenig, C. Tan, and R. Wang, "An automated estimator of image visual realism based on human cognition," in *Proc. IEEE Conf. Comput. Vis. Pattern Recognit.*, vol. 2, 2014.

[52] Y. Agam and R. Sekuler, "Interactions between working memory and visual perception: An ERP/EEG study," *Neuroimage*, vol. 36, no. 3, pp. 933–942, 2007.

[53] R. L. Buckner, M. E. Raichle, F. M. Miezin, and S. E. Petersen, "Functional anatomic studies of memory retrieval for auditory words and visual pictures," *Journal of Neuroscience*, vol. 16, no. 19, pp. 6219–6235, 1996.

[54] G. Seber and C. Wild, *Nonlinear Regression*, ser. Wiley Series in Probability and Statistics. Wiley, 2003.

[55] C.-C. Chang and C.-J. Lin, "Libsvm: A library for support vector machines," *ACM Trans. Intell. Syst. Technol.*, vol. 2, no. 3, pp. 27:1–27:27, May 2011.

[56] C.-W. Hsu, C.-C. Chang, and C.-J. Lin, "A practical guide to support vector classification," Department of Computer Science, National Taiwan University, Tech. Rep., 2003. [Online]. Available: http://www.csie.ntu.edu.tw/~cjlin/papers/guide/guide.pdf

[57] P. Zhang, "Model selection via multifold cross validation," *Annals of Statistics*, vol. 21, no. 1, pp. 299–313, 1993.

[58] J. Kittler, M. Hatef, R. P. W. Duin, and J. Matas, "On combining classifiers," *IEEE Trans. Pattern Anal. Mach. Intell.*, vol. 20, no. 3, pp. 226–239, Mar 1998.

[59] A. Kale, A. Roychowdhury, and R. Chellappa, "Fusion of gait and face for human identification," in *Proc. IEEE Int. Conf. Acoust., Speech, and Signal Process.*, vol. 5, May 2004, pp. V–901–4 vol.5.

[60] A. Mittal, G. S. Muralidhar, J. Ghosh, and A. C. Bovik, "Blind image quality assessment without human training using latent quality factors," *IEEE Signal Process. Lett.*, vol. 19, no. 2, pp. 75–78, Feb. 2012.

[61] X. Gao, F. Gao, D. Tao, and X. Li, "Universal blind image quality assessment metrics via natural scene statistics and multiple kernel learning," *IEEE Trans. on Neural Netw. and Learn. Syst.*, vol. 24, no. 12, pp. 2013–2026, Dec 2013.

[62] A. Mittal, A. Moorthy, and A. Bovik, "No-reference image quality assessment in the spatial domain," *IEEE Trans. Image Process.*, vol. 21, no. 12, pp. 4695–4708, Dec 2012.

[63] D. J. Sheskin, *Handbook of parametric and nonparametric statistical procedures*. CRC Press, 2003.

[64] S. A. Dudani, "The distance-weighted k-nearest-neighbor rule," *IEEE Trans. Syst., Man, Cybern.*, no. 4, pp. 325–327, 1976.

[65] K. E. A. Van de Sande, T. Gevers, and C. G. M. Snoek, "Evaluating color descriptors for object and scene recognition," *IEEE Trans. Pattern Anal. Mach. Intell.*, vol. 32, no. 9, pp. 1582–1596, Sept 2010.

[66] N.-X. Lian, V. Zagorodnov, and Y.-P. Tan, "Color image denoising using wavelets and minimum cut analysis," *IEEE Signal Process. Lett.*, vol. 12, no. 11, pp. 741–744, Nov 2005.

[67] K. Dabov, A. Foi, V. Katkovnik, and K. Egiazarian, "Color image denoising via sparse 3d collaborative filtering with grouping constraint in luminance-chrominance space," in *Proc. IEEE Int. Conf. Image Process.*, vol. 1, Sept 2007, pp. I – 313–I – 316.

[68] Z. Wang, E. Simoncelli, and A. Bovik, "Multiscale structural similarity for image quality assessment," in *Proc. IEEE Asilomar Conf. Signals, Systems and Comput.*, vol. 2, Nov 2003, pp. 1398–1402 Vol.2.